Comparisons of the Data-Driven D Region (D3R) Model to Incoherent Scatter Radar Observations During the Active Solar Conditions of September 2017

Austin Egert[1], James V. Eccles[1], Jeffrey M. Holmes[2], and Joseph Malins[2]

[1]Space Dynamics Laboratory, North Logan, UT, USA
[2]Air Force Research Laboratory, Kirtland AFB, NM, USA

Corresponding Author: austin.egert@sdl.usu.edu

ABSTRACT

The physics-based Data-Driven D Region (D3R) model calculates electron density profiles from 36 km to 134 km for quiet time and disturbed conditions. We compare D3R E and D region electron density profiles and high-frequency absorption predictions against available ISR observations during the active solar period of September 2017. Data from the Millstone Hill, Tromsø EISCAT, and Svalbard EISCAT ISRs provide electron density profiles during September 2017.

1. INTRODUCTION

This work focuses on comparisons between incoherent scatter radar (ISR) data and model results in the D and E regions of the ionosphere. Data collected from the Millstone Hill, Tromsø EISCAT (European Incoherent Scatter Scientific Association), and Svalbard EISCAT ISRs provide the observational backdrop against our D-region model. We use the updated Data-Driven D Region (D3R) model of *Eccles et al.* [2005] to calculate comprehensive time-dependent electron density profiles. The species and chemistry executed in the D3R model resemble the eight-component scheme presented in *Bekker et al.* [2022]. We focus on the active solar flare period of 6-11 September 2017 comparing model results with observations of x-ray flares (XRFs) and solar proton events (SPEs) during this time period.

2. D3R MODEL OVERVIEW

The D3R model provides a time-dependent solution of electron density profiles based on simplified D-region chemistry from 34 km to 132 km in 2-km altitude steps. The D3R model computes the detailed ionization profiles generated by solar x-ray fluxes, extreme ultraviolet fluxes, and Lyman Alpha ultraviolet flux through the Flare Irradiance Spectral Model-Version 2 (FISM2) [*Chamberlin et al*., 2020], and energetic particle ionization from solar energetic protons, auroral electron precipitation, and galactic cosmic rays [*Heaps*, 1978]. Secondary electron contributions to ionization follow the approach presented in *Rasmussen et al.* [1988] by assuming the energy of photons and energetic particles produces one electron-ion pair per 35 eV of energy available [*Banks and Kockarts*, 1973]. The time-dependent solution of the chemistry using the continuity equation for each species with no transport is given by

$$\frac{\partial n_s}{\partial t} = P_s - L_s n_s$$

where n_s is the number density of species s, P_s represents the total ionization production rate, and L_s represents the loss rate. There are eight species included (e, O^+, N_2^+, NO^+, O_2^+, XY^+, O_2^-, XY^-) to represent the ion-electron reactive system of the D region. XY^+ is the representative large molecular positive ion species with a fast recombination (e.g., O_4^+, N_4^+, hydrate ions, etc.). XY^- is used to represent the long-lived stable negative ions. The neutral atmosphere temperatures and constituent densities (N, O, N_2, NO, and O_2) are provided by the Naval Research Laboratory Mass Spectrometer Incoherent Scatter radar, version 2.1, (NRLMSIS 2.1) model [*Emmert et al.*, 2022]. The electron and ion temperatures are set to the neutral temperature. The metastable $O_2(^1\Delta_g)$ density is calculated based on formulae from *Swider and Foley* [1978].

3. ISR DATA OVERVIEW

Data collected from the Tromsø EISCAT, Svalbard EISCAT, and Millstone Hill ISRs were obtained from the Coupling, Energetics, and Dynamics of Atmospheric Regions (CEDAR) Program Madrigal Database website. Additionally, Geostationary Operational Environmental Satellite (GOES) data from the Laboratory for Atmospheric and Space Physics (LASP) Space Weather Data Portal are also shown to identify flares and solar proton events. A summary of event peaks during our time of interest is listed in Table 1. The SPE that occurred on 10 September continued to deposit protons into the ionosphere for more than three days.

Table 1. Summary of solar event times. Times listed are for the peak value, not the start of the event.

Flares (X-Class)	Solar Proton Events
06 Sep, 09:39 UTC	06 Sep, 23:50 UTC
06 Sep, 12:04 UTC	07 Sep, 23:25 UTC
07 Sep, 10:19 UTC	08 Sep, 12:40 UTC
07 Sep, 14:39 UTC	08 Sep, 13:05 UTC
08 Sep, 07:49 UTC	08 Sep, 16:40 UTC
10 Sep, 16:06 UTC	10 Sep, 17:15 UTC*

*In this case, the time is for onset.

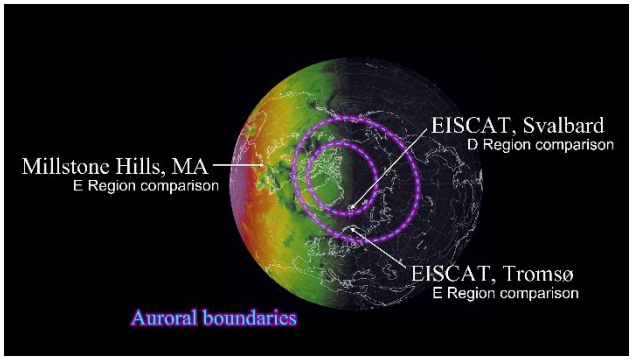

Figure 1. Locations of the ISRs included in this paper. The approximate auroral oval boundaries are shown for reference. The image was adapted from earth (earth.nullschool.net).

The ISR locations providing the data investigated in this paper are shown in Figure 1. The auroral oval boundaries and dayside illumination are included to demonstrate the SPE and XRF regions of greatest effect, respectively. The XRFs impact the EISCAT sites only weakly due to their high-latitude location. Alternatively, the SPEs do not significantly influence the Millstone Hill site due to its lower magnetic latitude.

Figure 2 shows the x-ray flux and the solar proton flux during 4-17 September 2017. Various high-magnitude peaks are visible in the x-ray flux, demarking the solar XRFs. Several large SPEs are also visible, particularly the prolonged event beginning on the 10th. Figure 3 shows the expanded view for 6-11 September highlighted in Figure 2 by the red box. Vertical red lines mark the XRFs, and vertical cyan lines mark the SPEs.

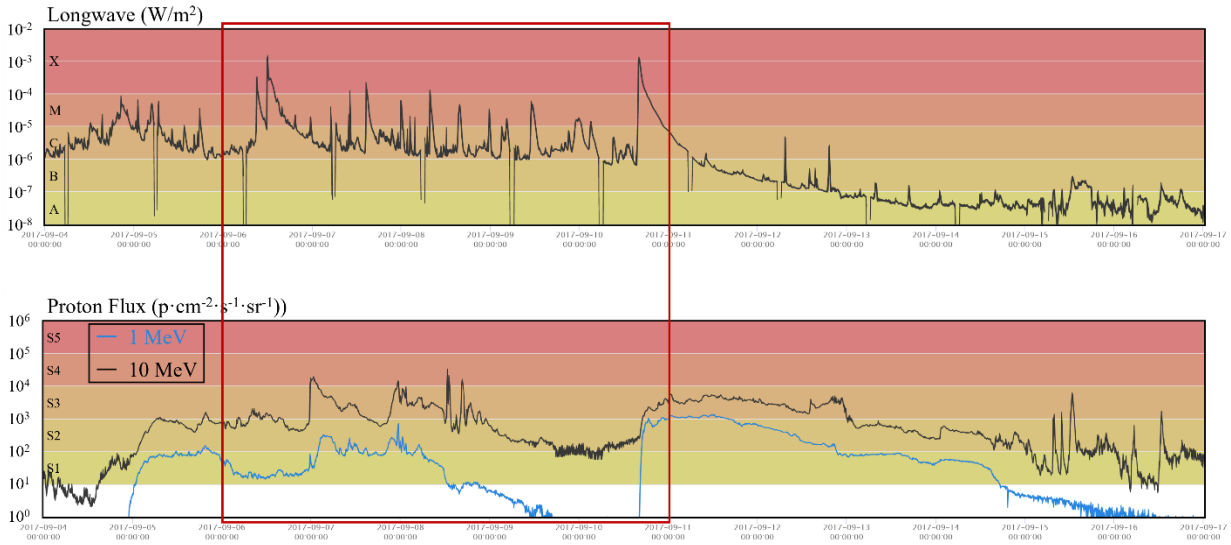

Figure 2. Solar x-ray flux (top) and solar proton flux (bottom) from 4-17 September 2017. This paper primarily focuses on the 6-11 September timeframe (red box). The data are taken from the LASP Space Weather Data Portal.

Figure 3. Solar x-ray flux (top) and solar proton flux (bottom) from 6-11 September 2017 highlighted by the red box in Figure 2. A few X-class flares (vertical red lines) and many M-class flares (peaking in the orange) occurred during this time. Additionally, several large SPEs (vertical cyan lines) occurred within the same timeframe.

Figure 4.a. illustrates the time history of electron density at 106.9 km (cyan), with the proton flux (magenta) and the K_p index (blue dotted), for the Tromsø EISCAT ISR. The impact by XRFs is just visible on 6 September at about 10:00 UT and 12:00 UT, and to a lesser degree, on 7 September near 12:00 UT. Much of the density enhancement (for example, on 8 September) is due to the solar proton flux reaching the ionosphere along the magnetic field lines and auroral precipitation with increased K_p. Figure 4.b. shows the time history of electron density for the Millstone Hill ISR at 104.0 km (red) along with the x-ray flux (black) and the $F_{10.7}$ index (blue dashed). Multiple flare enhancements occur during this time period, with notable examples on 6 September at 12:00 UT and 10 September at 17:00 UT.

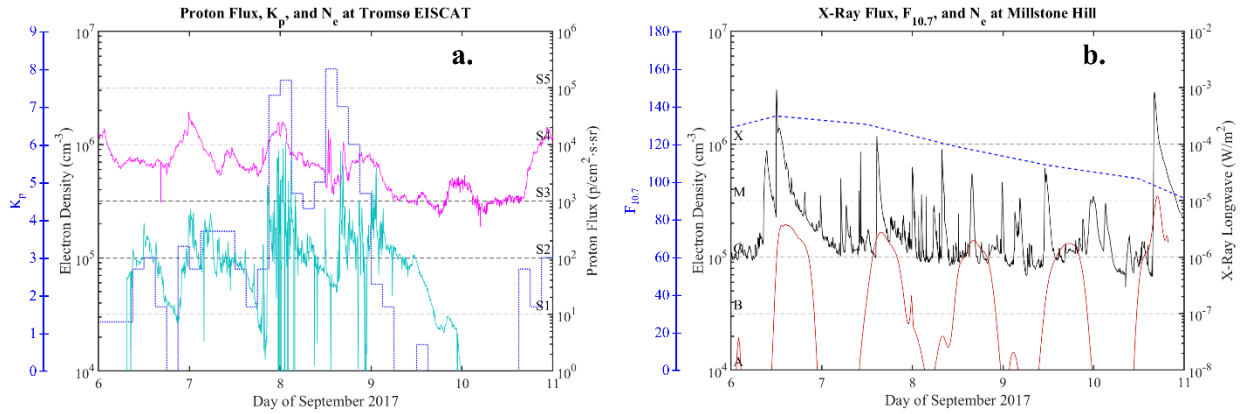

Figure 4. (Figure 4.a.) Electron densities for the Tromsø EISCAT at an altitude of 106.9 km (cyan) with the proton flux (magenta) and the K_p index (blue dotted). (Figure 4.b.) Electron densities for the Millstone Hill ISR at an altitude of 104.0 km (red) with the x-ray flux (black) and the $F_{10.7}$ index (blue dashed). The impact by the flares is visible on the 6th at about 10 UT and 12 UT. Density enhancements related to the solar proton flux are evident. SPE and XRF data are taken from the GOES database.

4. MODEL AND COMPARISONS

D3R assimilated x-ray flux and solar proton flux data to model the observational electron density profiles at the three ISR sites. Figure 5 shows the comparison between the electron density calculations by D3R (top left) and the observations by the Svalbard EISCAT ISR (top right) for a 5-hour period on 6 September. The x-ray flux data (bottom left) highlight the X-class flare peak at 12:00 UT. Its impact on the D region is visible in the density profiles, where the ions and electrons gradually recombine as the x-ray flux relaxes. The model and data density profiles are compared at the peak of this flare (bottom right), demonstrating a similar shape and magnitude of the D3R (red) and the ISR data (blue). The D3R electron densities are slightly less than observed densities at all altitudes for this X-class solar flare peak time.

Figure 6 shows the comparison between Tromsø EISCAT ISR observations at 106.9 km (cyan) and D3R results at 106.0 km (black). The electron density calculated by D3R is strongly modified by the solar proton flux and auroral precipitation with smaller contributions from the x-ray flux throughout the 3-day period. Although D3R captures the average trend, the results are often lower than observations.

For dayside electron density profiles, D3R captures the strong influence in the D and E regions caused by XRFs. Millstone Hill ISR data were not available for altitudes below 100 km, so the comparison with D3R is limited to E-region altitudes. Figure 7 shows the comparison between observations (blue) and D3R results at 128.0 km (black). Enhancement by XRFs appears more dramatic in the D3R results, for example, on 6 September at 12:00 UT and 10 September at 17:00 UT. The smoother enhancements in observations may stem from complex chemistry with upward transport from the E region densities not captured in the D3R architecture.

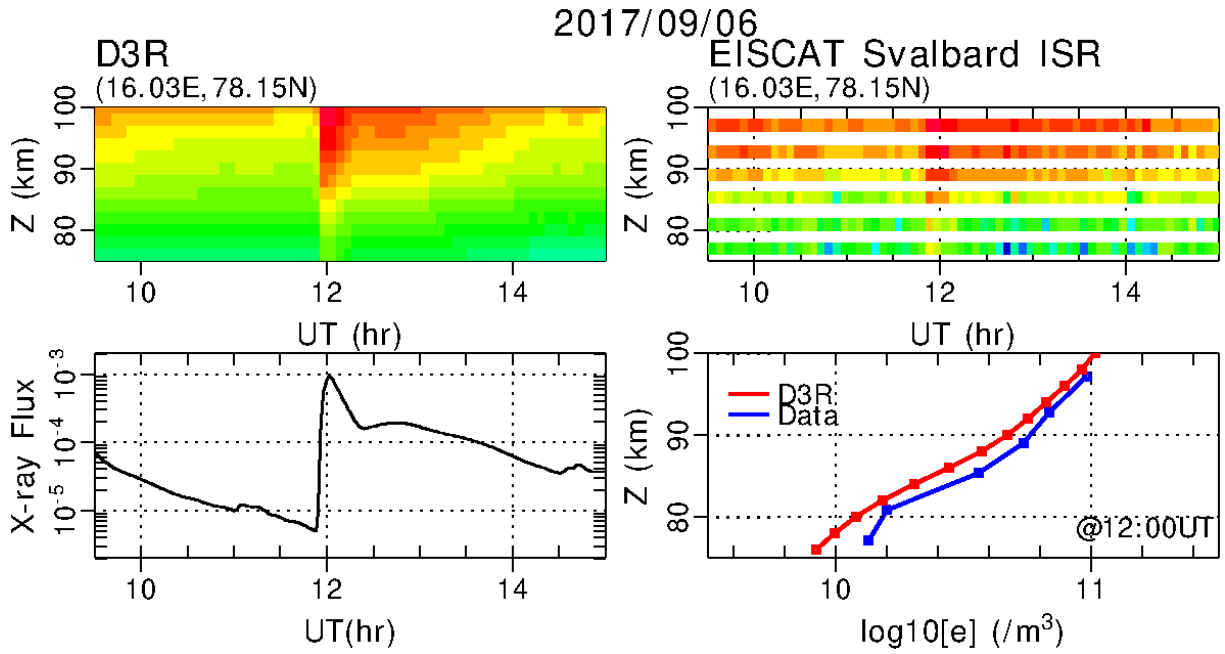

Figure 5. Electron density D3R calculations (top left) and ISR observations (top right) for 6 September 2017. The XRF (bottom left) influence can be seen in the density profiles. The density profile comparison at 12:00 UT (bottom right) shows the similar shape between D3R (red) and the ISR data (blue).

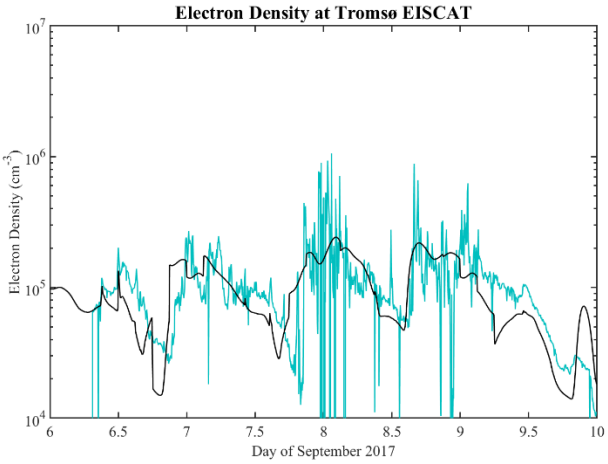

Figure 6. Electron density profile comparison for the Tromsø EISCAT between observations at 106.9 km (cyan) and D3R results at 106.0 km (black). Magnitudes of the D3R results are predominantly lower than observations, but the basic trend over time is similar.

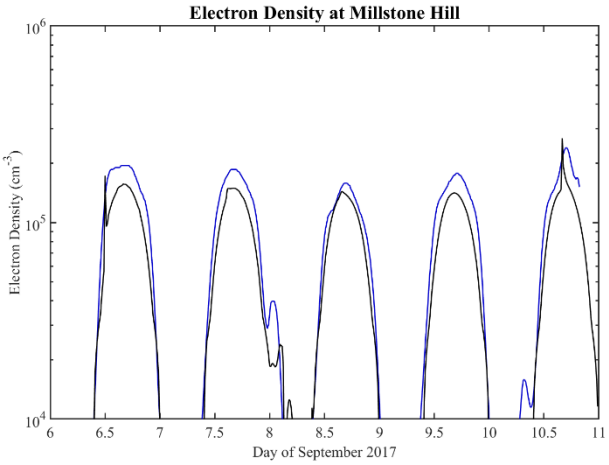

Figure 7. Electron density profile comparison for the Millstone Hill ISR between observations (blue) and D3R results (black) at 128.0 km. The flare enhancement can be seen on 6 September at 12:00 UT and 10 September at 17:00 UT.

5. CONCLUSION

While this current configuration of the D3R model captures ionospheric enhancement by XRFs, SPEs, and auroral precipitation, weighting each impact with geographic and geomagnetic location, the calculated electron densities consistently underestimate the observations in the D and E regions for XRF periods. Including transport in the D3R architecture may improve its accuracy for E region densities. Increased availability of ISR data at altitudes below 100 km may prove insightful for D region model comparisons.

ACKNOWLEDGEMENTS

This work was funded by the Office of Naval Research and the Air Force Research Laboratory contract FA9453-22-F-0009. The authors would like to thank the LASP Space Weather Data Portal (lasp.colorado.edu/space-weather-portal) for collecting and organizing the GOES data in readily usable formats. We would like to thank Dr. Phil Erickson of MIT Haystack Observatory for providing the Millstone Hill ISR data and Dr. Ingemar Häggström of the EISCAT Scientific Association for providing the EISCAT ISR data to the CEDAR Madrigal Database website (https://cedar.openmadrigal.org). These results presented rely on the FISM2 model described in *Chamberlin et al.* [2020] cited below. These data were accessed via the LASP website (https://lasp.colorado.eud/lisird). The authors would also like to thank earth.nullschool.net for the excellent graphics of their weather model at https://earth.nullschool.net.

Approved for public release; distribution is unlimited. Public Affairs release AFRL-2023-1743. The views expressed are those of the authors and do not reflect the official guidance or position of the United States Government, the Department of Defense or of the United States Air Force. Statement from DoD: The appearance of external hyperlinks does not constitute endorsement by the United States Department of Defense (DoD) of the linked websites, or the information, products, or services contained therein. The DoD does not exercise any editorial, security, or other control over the information you may find at these locations.

REFERENCES

Banks, P.M. & G. Kockarts (1973), Aeronomy, Academic Press, New York, NY, 1973

Bekker, S. Z., S. I. Kozlov, & V. P. Kudryavcev (2022). Comparison and verification of different schemes for the ionization-recombination cycle of the ionospheric D-region, J. Geophys. Res.: Space Physics, 127(10), e2022JA030579. https://doi.org/10.1029/2022JA030579

Chamberlin, P. C., F. G. Eparvier, V. Knoer, et al. (2020). The Flare Irradiance Spectral Model-Version 2 (FISM2), Space Weather, 18(12), e2020SW002588. https://doi.org/10.1029/2020SW002588

Eccles, J. V., R. D. Hunsucker, D. Rice, et al. (2005). Space weather effects on midlatitude HF propagation paths: Observations and a data-driven D region model, Space Weather, 3(1), https://doi.org/10.1029/2004SW000094

Emmert, J. T., M. Jones Jr, D. E. Siskind, et al. (2022). NRLMSIS 2.1: An Empirical Model of Nitric Oxide Incorporated Into MSIS, J. Geophys. Res.: Space Physics, 127(10), e2022JA030896. https://doi.org/10.1029/2022JA030896

Heaps, M. G. (1978). Parametrization of the cosmic ray ion-pair production rate above 18 km. Planetary and Space Science, 26(6), pp. 513-517. https://doi.org/10.1016/0032-0633(78)90041-7

Rasmussen, C. E., R. W. Schunk, & V. B. Wickwar (1988). A photochemical equilibrium model for ionospheric conductivity, J. Geophys. Res.: Atmospheres, 93(A9), 9831-9840. https://doi.org/10.1029/JA093iA09p09831

Swider, W & C. I. Foley (1978). Steady-State Multi-Ion Disturbed D-Region Model, AFGL-TR-78-0155, No. 636